Journal of Power Sources 227 (2013) 72–79

Contents lists available at SciVerse ScienceDirect

Journal of Power Sources

journal homepage: www.elsevier.com/locate/jpowsour

In situ measurement of temperature distribution in proton exchange membrane fuel cell I a hydrogen–air stack

Houchang Pei [a], Zhichun Liu [a], Haining Zhang [b], Yi Yu [b], Zhengkai Tu [b,*], Zhongmin Wan [a,c], Wei Liu [a,**]

[a] School of Energy and Power Engineering, Huazhong University of Science and Technology, Wuhan 430074, China
[b] State Key Laboratory of Advanced Technology for Materials Synthesis and Processing, Wuhan University of Technology, Wuhan 430070, China
[c] College of Information Engineering, Hunan Institute of Science and Technology, Yueyang 414006, China

HIGHLIGHTS

► Temperature was investigated in the stack by embedding 36 thermocouples.
► The temperature in the stack exhibited "Parabola" distribution.
► Elevated air and water flow rates improved the temperature distribution uniformity.

ARTICLE INFO

Article history:
Received 3 September 2012
Received in revised form
25 October 2012
Accepted 13 November 2012
Available online 20 November 2012

Keywords:
Proton exchange membrane fuel cell
Temperature distribution
Thermocouples
Stack

ABSTRACT

Temperature mapping is measured by micro-thermocouples embedded into the cathode plate of the model cell. The effects of different operation conditions on temperature distribution are investigated in detail. The results show that the temperature of the stack turns on "Parabola" distribution, and the temperature increases along the flow field from the inlet to the outlet under various conditions. Temperature difference of the single cell in the stack increases with the increased operation current density, and decreases with the increased air flow rate. The effect of the inlet air temperature on the temperature difference can be neglected in the stack, and the temperature uniformity can be improved by increasing the mass flow rate of the coolant water.

1. Introduction

Proton exchange membrane fuel cell (PEMFC) is a power device which transfers chemic energy contained in hydrogen and oxidant into electrical energy directly [1–9]. Since nearly half of the released energy is transferred to thermal energy in the stack during its operation, large asymmetry temperature gradient will generate in PEMFC without proper thermal management [10–13]. The increased temperature of the cell makes the membrane to be dehydrated and lowers the proton conductivity of the membrane, leading to poor performance of the stack and eventually irreversible damage. On the other hand, the catalyst cannot carry out its best activity at the low temperature area in the MEA (membrane electrode assembly) and non-uniformity current density distribution will generate in the cell. In addition, low temperature can also result in water condensation or even flooding, causing the performance deterioration of the cell during its operation [14,15]. In situ measurement of temperature distribution is essential for better understanding of the real-time characteristics, and for the optimization design and operation in PEMFC.

Tremendous research efforts have been conducted on temperature measurement in PEMFC. The measurement methods can be divided into, in-fiber Bragg grating sensor [16], thermistor [17,18], infrared thermography [19–22], band-gap temperature sensor [23], and the most widely used approach of embedding the thermocouples into the cell directly [24–30]. Prinz [24] used micron and millimeter scale sensors to acquire the temporal distributions of temperature, oxygen partial pressure, and relative humidity in the mass transport layer in an air-breathing fuel cell. The spatial resolution and the temporal resolution of the sensors are approximately 1 mm or better and 1 s, respectively. The result showed that the cell's cathode rib structure visibly influenced oxygen distribution, and thermal and species concentration effects could be extended beyond the cathode surface, into the surrounding space. Ohsaka [25] addressed the polarization behaviors of five segmented fuel cells with Nafion 112 membrane as the catalysts'

* Corresponding author. Fax: +86 27 87879468.
** Corresponding author. Fax: +86 27 87540724.
E-mail addresses: tzklq@whut.edu.cn (Z. Tu), wei_liu@hust.edu.cn (W. Liu).

0378-7753/$ – see front matter © 2012 Elsevier B.V. All rights reserved.
http://dx.doi.org/10.1016/j.jpowsour.2012.11.027

support in one fuel cell compartment. The results showed that the temperature gradient existed and it depended on the gases' flow direction in these five fuel cells. The temperature differences generated even at zero current load due to the hydrogen crossover. Maranzana [26] tested the performance in a multi-instrumented transparent single PEMFC, and they also found that temperature field was strongly correlated with the current density distribution and both depended strongly on water management. The local aging effects existed due to the hydrogen crossover, which might have consequences on reliability of the fuel cell. Wilkinson [27] sets 17 thermocouples in the landing widths of the flow fields in the active area to measure the current density distribution according to the in situ temperature variety. The current mapping could be indirectly conducted through local temperature measurements, and this method provided in situ high-resolution data capable of following load cycling and could be used in real applications. Sasaki [28] inserted 7 micro-thermocouples between the gas diffusion layer and membrane electrode assembly to monitor the temperature distribution in a PEMFC. They pointed out that insertion of micro-thermocouples did not have a large influence on the cell performance. It was observed that the electrochemistry reaction could be considered to be main heat source during the operation and the cathode catalyst layer reached the maximum temperature. Contrarily, it had the minimum temperature just after the load current was stopped due to the evaporation of the liquid water generated in the cell. Wen [29] investigated the temperature distribution in a transparent PEMFC by embedding 11 thermocouples into the cathode gas channel plate fabricated with high thermal conductivity pyrolytic graphite sheet (PGS), and they found that the location of liquid water was correlated with the temperature measurement. Compared with the cell without PGS, temperature distribution was more uniform in the one with PGS, and the utilization of the PGS could reduce the maximum cell temperature and improve cell performance at high cathode flow rates. Kjelstrup [30] introduced 4 thermocouples into the gas channels and both sides of the membrane in a single fuel cell. Higher temperatures about 5 °C or more were monitored at the membrane electrode surface than in the gas channels at 1000 mA cm^{-2} and it was also found that the thermal conductivity of the membrane and the heat transfer coefficient of the electrode surfaces were both very small during the operation.

Although numerous works related to the temperature distribution in the fuel cell have been done in the past decades. However, the research objects above were all focused on a small single cell with low output power and no literature about the in situ temperature distribution in a PEMFC stack was reported. Compared with a single cell, hundred times of the generated heat needs to be removed by the coolant water and the coupling effects of every single cell itself along with the coolant components on the temperature distribution are more complicated. Thus, temperature characteristic in a PEMFC stack deserved more detailed works for practical applications. Therefore, the objective of this work is to investigate the in situ temperature distribution in a hydrogen–air PEMFC stack by embedding 40 thermocouples between the GDL surfaces and the coolant water inlet and outlet.

2. Experiments

The PEM fuel cell stack used in this study is composed of 46 single cells with straight-channel flow field. The anode and cathode plates are made from commercially available graphite material, which is hydrophobic with a low-electrical resistivity of about 100 μS cm^{-1} (in-plane). Anode and cathode flow field configurations are manufactured by a 3D numerical machine with the accuracy of ±0.01 mm [22]. The coolant flow channels have the same parameters with the cathode and anode flow fields. Geometrical properties of PEMFC stack are listed in Table 1. The used MEAs (Membrane Electrode Assemblies) consisted of the Nafion® 211 membrane in combination with platinum loadings of 0.4 mg cm^{-2} per electrode and the stack is cooled by the deionized water at a pre-set temperature. The performance of the stack was carried out on FCATS G500 produced by Greenlight Innovation Company in Canada. It could be programmed precisely to control various operational parameters, including electronic load, gas flow rate or stoichiometry, dew point temperature, inlet/outlet pressures, relative humidity (RH), and cell temperature. The schematic diagram of the test system for PEMFC stack is shown in Fig. 1.

Generally, to monitor the temperature, thermocouples should be placed near the cathode catalyst layer where they are closest to the heat source due to electrochemical reaction. Considering insertion of the thermocouples near the catalyst layer could increase mass transfer resistance in the areas and result in concentration losses in the overall and local performance of a PEMFC [31], thermocouples used to monitor the stack temperature in this experiment are placed between the rib of the flow channel and the gas diffuse layer (GDL) surface, as shown in Fig. 2(a).

There are four marked cells with thermocouples to investigate the temperature distribution characteristic in the 46 cells' fuel cell stack, and they are the first, the eleventh, the twenty-third and the forty-sixth single cell along the hydrogen inlet flow direction, respectively, as shown in Fig. 2(b). To study the in-plain temperature distribution there are nine T type thermocouples divided into three triads and placed in the inlet, three thermocouples placed in the top, middle and bottom at every marked cell, respectively, and denoted as TC1 ~ TC36, as shown in Fig. 2(c).

In each single cell, the cell operating temperature is measured by the thermocouple in the cathode endplate, whereas in a PEMFC stack, it is determined by the outlet temperature of the coolant water. To monitor the temperature variety of the coolant water, two thermocouples denoted as TC37 and TC38 are located in the coolant water inlet and outlet, respectively. In order to investigate effect of the air flow property on the temperature distribution, the inlet and outlet temperatures of the air are monitored by thermocouples of TC39 and TC40, respectively. The temperature range and accuracy of all the T type thermocouples used in the measurement are −200 to 350 °C and ±0.1 °C, respectively. The T type thermocouples are all connected to a data acquisition system (Keithlet-2700) for temperature monitored, and the sampling rate of each channel is set at 12 samples per minute. The purity of the hydrogen used in the test is 99.99%. The environmental temperature is 9 °C, and hydrogen and air are both fully humidified at the inlet temperature of 65 °C in Sections 3.1–3.3, and 3.5. For all measurements, both the anode and cathode are exhausting at the atmosphere directly.

3. Results and discussions

3.1. Single cell temperature distribution

Fig. 3 shows the temperature evaluation of the marked cells at the current density of 500 mA cm^{-2} with respect to the flow rates of

Table 1
Geometrical properties of PEM fuel cell stack.

Single cell area of this stack (m^2)	200×10^{-4}
Flow field depth (m)	7.5×10^{-4}
Flow field width (m)	1.5×10^{-3}
Flow field ridge width (m)	1.5×10^{-3}
Gas diffusion layer thickness (m)	2.5×10^{-4}
PEM thickness (m)	2.5×10^{-5}
Catalyst layer thickness (m)	1.2×10^{-5}

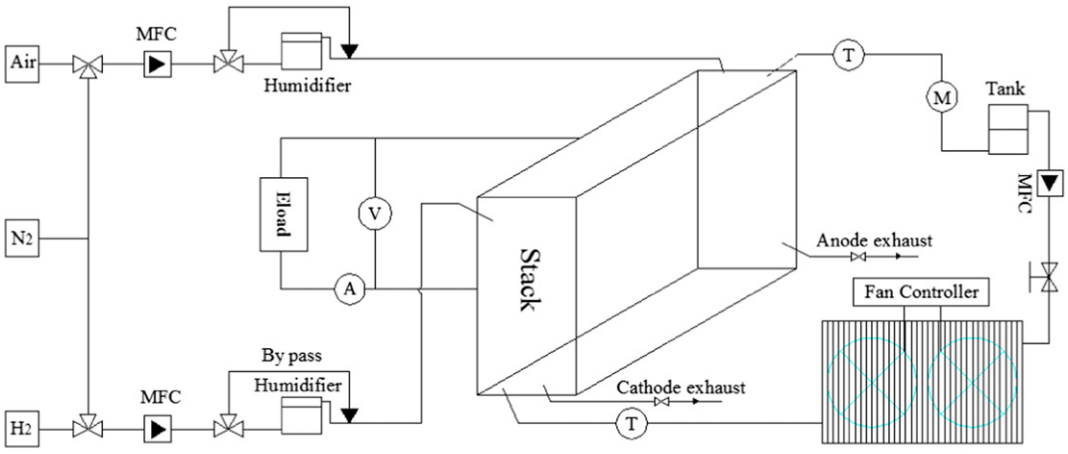

Fig. 1. Schematic diagram of the test system for PEMFC stack.

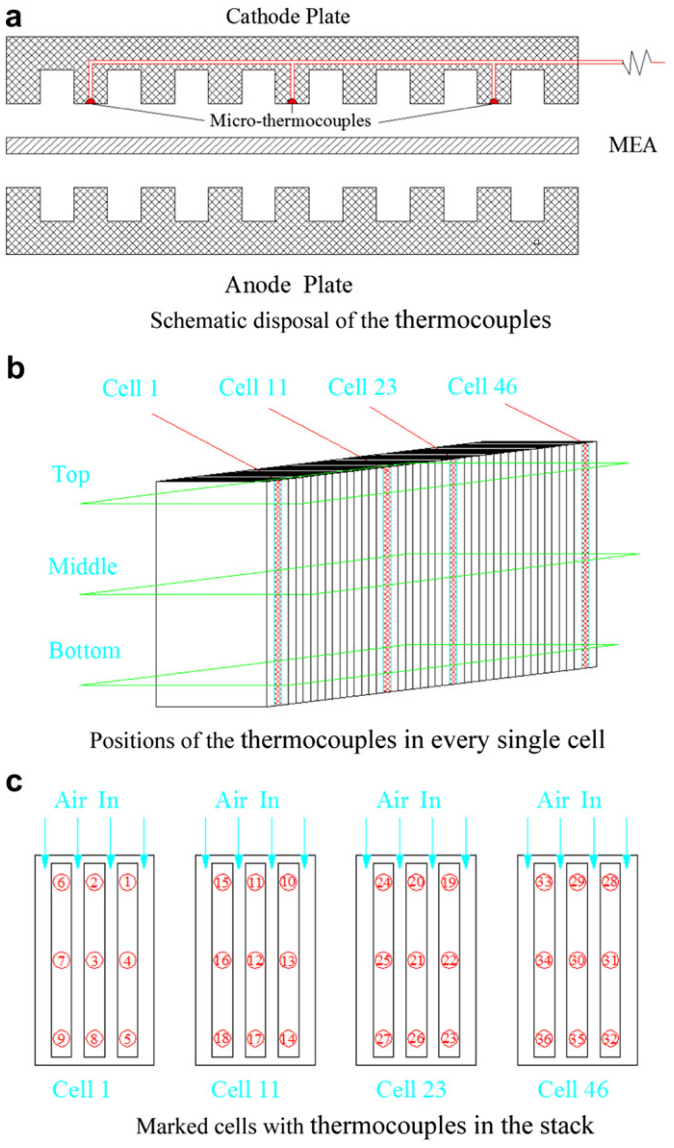

Fig. 2. Schematic positions of the thermocouples and marked cells in the stack. (a) Schematic disposal of the thermocouples. (b) Positions of the thermocouples in every single cell. (c) Marked cells with thermocouples in the stack.

the hydrogen, air, and coolant water of 50 NLPM, 500 NLPM and 45 NLPM, respectively. All the monitored temperatures increase with the time evolution. The highest temperature in each single cell is TC8, TC17, TC26 and TC35, respectively, and they are all located at the bottom-middle of the cell. The highest temperature was monitored by TC26 located in cell 23 in the middle of the stack. Although the lowest temperature was appeared in cell 1, it has nearly the same temperature distribution characteristic with that in cell 46. Meanwhile, the maximum temperature difference of stack can be calculated to be 5 °C by TC23 and TC1 (or TC46). The minimum temperature difference was observed in cell 46 or cell 1, and the value was within 1 °C. The similar temperature distribution tendency also appeared at 700 mA cm^{-2}. The main reason was that, the generated heat in the stack was mainly used for heating the coolant water and stack itself, and the different temperature differences among cells were due to the un-uniformity of the heat exchange between the coolant water and every single cell.

3.2. Effect of current density on temperature distribution

Fig. 4 shows the temperature distribution of the marked cells at different current densities with respect to the flow rates of the hydrogen, air and coolant water of 50 NLPM, 500 NLPM and 45 NLPM, respectively. The maximum temperature difference and temperature elevated rate increase with increasing current density. As can be seen from Fig. 4(a), at 500 mA cm^{-2}, the highest temperature TC26 in the stack increased from 67.7 °C to 69.3 °C and the lowest temperature increased from 62.5°C to 64 °C with the elevated rate of about 0.16 °C min^{-1} during the 10 min operation. Meanwhile, the largest temperature difference in the single cell was 4.6 °C in cell 23, and the largest temperature difference in the stack was 5 °C as mentioned in previous section. In contrast, at current density of 700 mA cm^{-2}, as shown in Fig. 4(b), the highest temperature in the stack increased from 75.7 °C to 79.2 °C with the elevated rate of 0.35 °C min^{-1} and the lowest temperature increased from 67.7 °C to 69.8 °C with respect to elevated rate of 0.21 °C min^{-1} after 10 min. Moreover, the largest temperature difference appeared in single cell increased to 7.8 °C and it was 8.4 °C in the stack. As also can be seen, the coolant water temperature difference was about 1.0 °C at 500 mA cm^{-2} while the value was 1.4 °C as the current density increased to 700 mA cm^{-2}, which indicated that more generated heat was removed by the coolant water at higher current density.

Fig. 5 shows the temperature profile in the stack at $t = 500$ s with respect to different current densities. As can be seen, not only

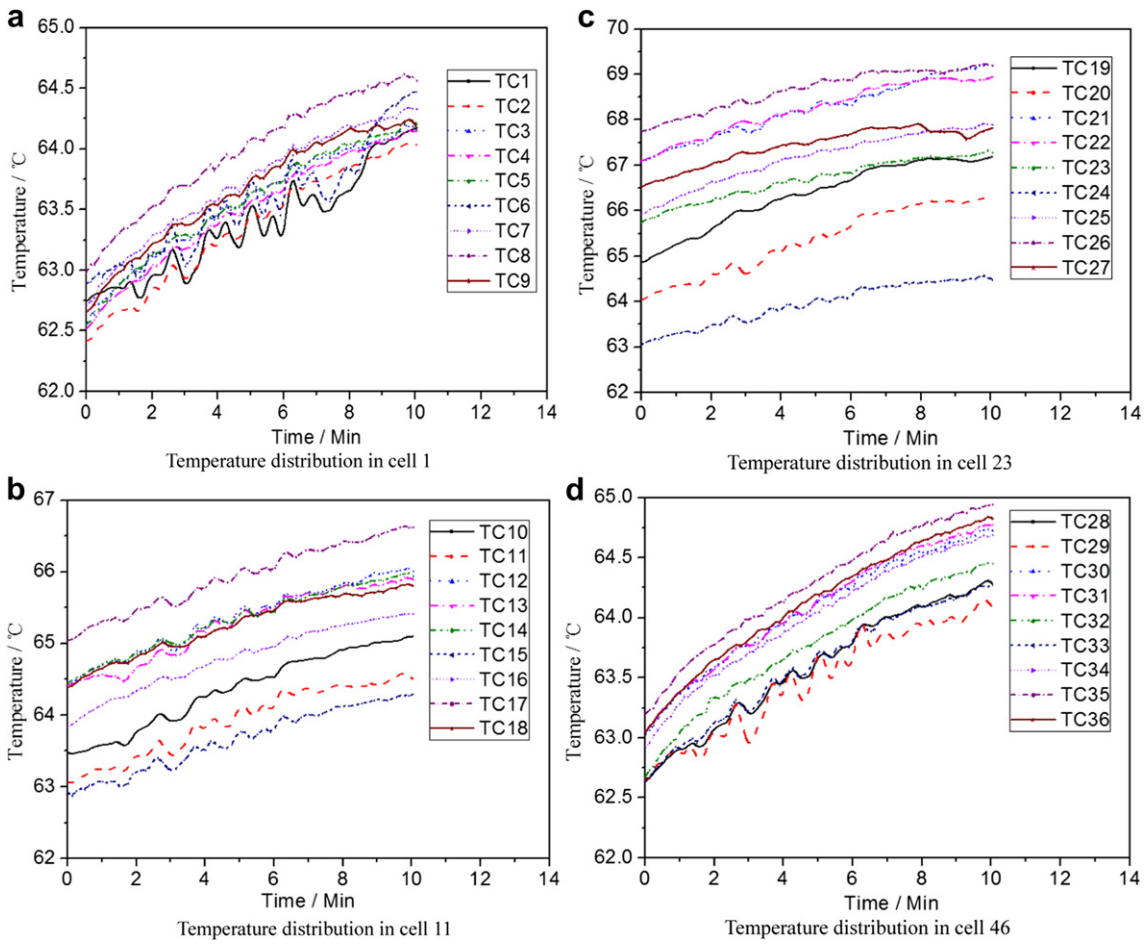

Fig. 3. Temperature distributions in different cells at 500 mA cm^{-2}. (a) Temperature distribution in cell 1. (b) Temperature distribution in cell 11. (c) Temperature distribution in cell 23. (d) Temperature distribution in cell 46.

the highest and lowest temperature, but also the temperature differences of the stack all exhibited a "Parabola" distribution at different current densities. At 500 mA cm^{-2}, temperature distribution of the lowest temperature in every single cell showed good uniformity, and the temperature differences were all within 1 °C. Meanwhile, the maximum temperature difference of the highest temperature in each single cell was no more than 4 °C. On the contrary, the lowest temperature difference of every single cell in the stack increased to 1.4 °C, and the highest temperature difference increased to 8 °C with increasing current density to 700 mA cm^{-2}. As mentioned above, the highest temperature was located in the middle of the stack. Therefore, special attention should be paid to the heat removal of the middle cells in the optimal design of the fuel cell stack to improve the temperature uniformity.

3.3. Effect of air flow rate on temperature distribution

Fig. 6 shows cell temperature distribution with different air flow rates at 500 mA cm^{-2} when the hydrogen and coolant water flow rates are 40 NLPM and 45 NLPM, respectively. Fig. 6(a) shows the temperature evolutions of every monitored thermocouple in the typical single cell 23 at different air flow rates. All the temperatures at monitored points increased with the time evolution at the air flow rates were 300 NLPM and 500 NLPM with temperature elevated rates were 0.098 °C min^{-1} and 0.062 °C min^{-1}, respectively. Moreover, when the air flow rate increased from 500 NLPM to 700 NLPM, the temperatures at every test position decreased at first and remained stable after 2 min. Therefore, air flow rate could affect the temperature distribution in PEMFC stack. First of all, the Reynolds number increased by increasing the air flow rate, and the mass transport coefficient between the air flow and PEM was enhanced. Accordingly, more generated water was blow out of the stack directly. Secondly, more generated heat was also removed out of the stack by the convective heat transfer between the air and bipolar plates at the elevated air flow rate. Thirdly, most of the water vapor with high enthalpy was blown out the stack in the moisture rapidly at elevated air flow velocity, and the exothermic process of condensation into liquid for the water vapor could not carry out in time. The reason for the increased temperature with respect to the air flow rates of 300 NLPM and 500 NLPM was that, the total heat removed by the coolant water and flowing air was less than that generated in the stack. Contrarily, the stack could reach the thermal balance when the air flow rate was 700 NLPM, and the heat generated in the stack was equal to that removed from the stack. The transient temperature decreased phenomena with respect to the air flow rate variation from 500 NLPM to 700 NLPM was that, on the one hand, the flow meter was carrying out the self-regulation to maintain the mass flow rate at 700 NLPM. On the other hand, coupling of heat and water transport ability was enhanced suddenly at the variety of the air flow rates and more heat was removed by the air flow.

Fig. 6(b) shows temperature difference distribution in the fuel cell stack. As can be seen, temperature difference at every single cell

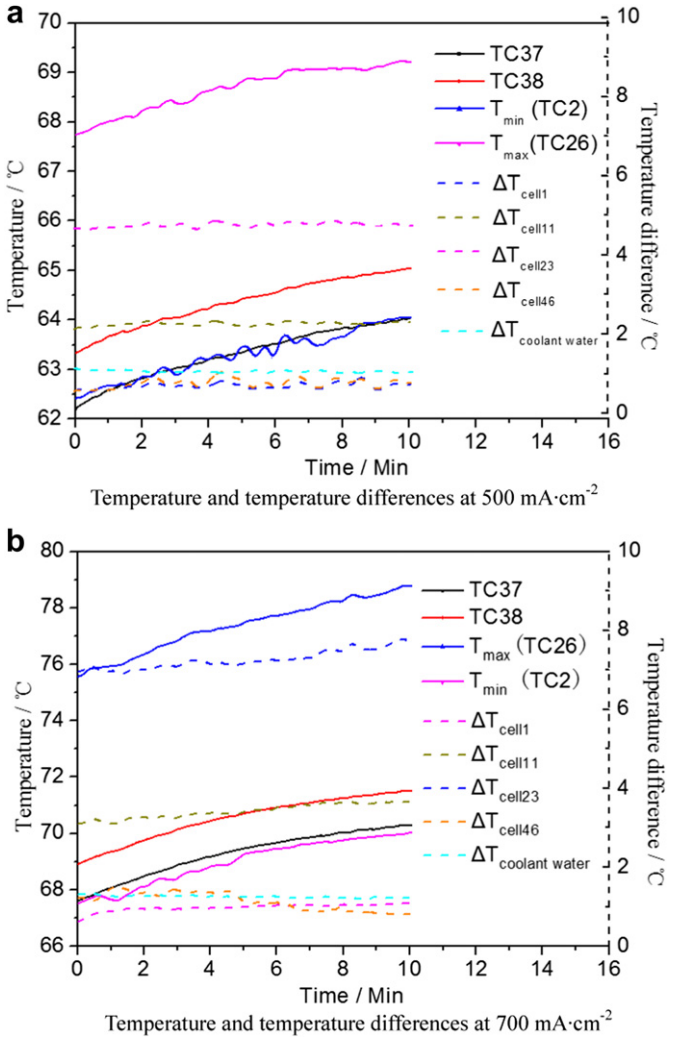

Fig. 4. Temperature and temperature differences distribution at different current densities. (a) Temperature and temperature differences at 500 mA cm^{-2}. (b) Temperature and temperature differences at 700 mA cm^{-2}.

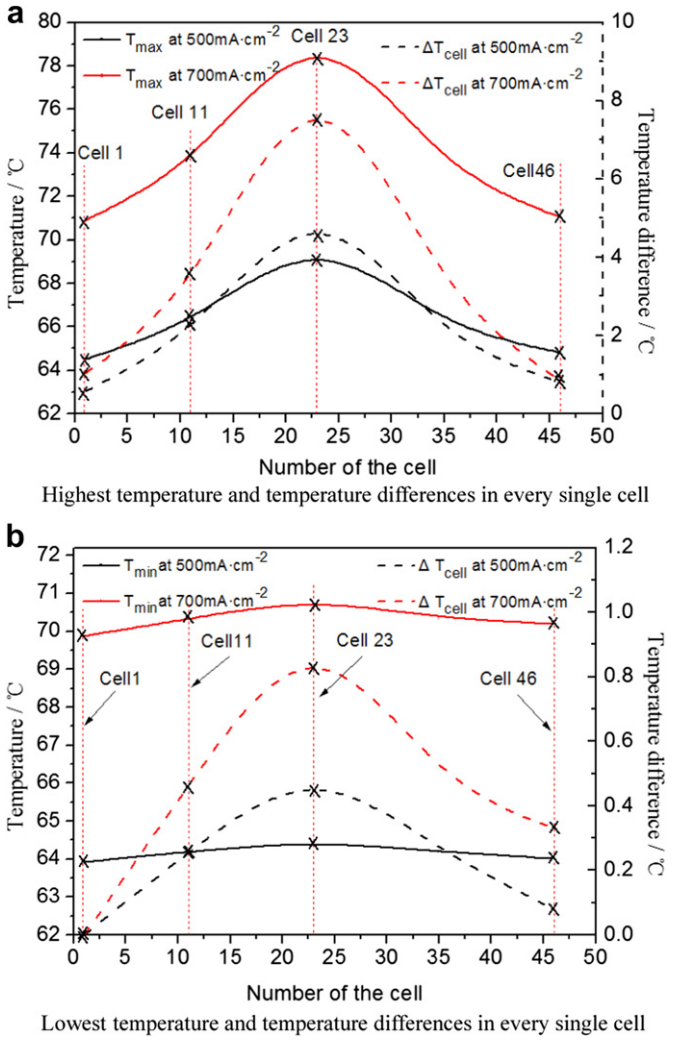

Fig. 5. The instantaneous temperature distribution in the stack at different current densities. (a) Highest temperature and temperature differences in every single cell. (b) Lowest temperature and temperature differences in every single cell.

decreased at larger air flow rate and the temperature distribution was more uniform with the increase in the air flow rate. The decreased air temperature difference at a lower air flow rate was due to the sufficient heat exchange between the air and the bipolar plates at the decreased flow rate of the air in the stack. Moreover, as also can be seen, more heat would generate in the stack at the lower mean voltage when the air flow rates were 300–500 NLPM, respectively, and larger temperature difference of the coolant water was generated to remove more heat from the stack. The increased air flow rate, on the one hand, increased the concentration of the oxidant, which could enhance the operation voltage of the stack, reduced the heat generated amount. On the other hand, it improved the water management. Accordingly, more liquid water accumulated in the GDL and catalyst layer (CL) evaporated into water vapor and was removed out of the stack by the flow air.

3.4. *Effect of air inlet temperature on temperature distribution*

Fig. 7 shows the cell temperature distribution with different air inlet temperatures at 500 mA cm^{-2} when the hydrogen, air and coolant water flow rates are 40 NLPM, 500 NLPM and 45 NLPM, respectively. Both hydrogen and air are fully humidified with the inlet temperatures of 85 °C, 55 °C and 40 °C. Fig. 7(a) shows the temperature evolutions of the monitored thermocouples in cell 23. All the temperatures increased slightly when the inlet air temperature was 85 °C. Contrarily, they decreased rapidly at 55 °C and 40 °C, respectively. Meanwhile, the temperature decrease rate of every thermocouple was equal to 0.28 °C min^{-1} and the temperature difference in the cell remained at about 5–6 °C with respect to the inlet air temperature of 55 °C whereas nearly the same temperature difference could be observed at 85 °C and 40 °C. Hence, there was little influence of inlet air temperature on the temperature difference in the fuel cell stack. Moreover, as can be seen in Fig. 7(b), the temperature differences of the coolant water were almost the same at three inlet air temperatures, and the according heat removed by the coolant water was equivalent. The slight increase in temperature in the cell was attributed to the higher inlet air temperature compared to the coolant water temperature (named stack temperature), which would heat the stack. On the contrary, the low temperature inlet air would play a cooling effect on the stack, and the temperatures, including the inlet and outlet temperatures of the coolant water, would all decrease immediately at the decreased inlet temperature. Besides, a notable phenomena was that, a large positive temperature difference of 16.5 °C between the inlet and outlet air generated when the inlet air temperature was 85 °C, and it became negative

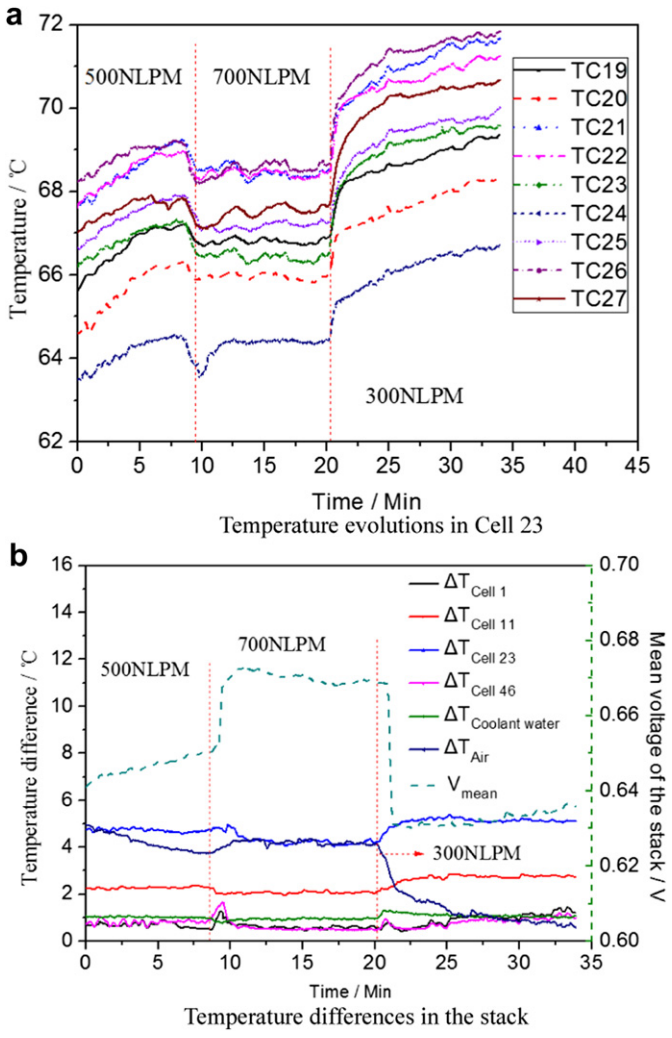

Fig. 6. Temperature distribution at different air flow rates. (a) Temperature evolutions in cell 23. (b) Temperature differences in the stack.

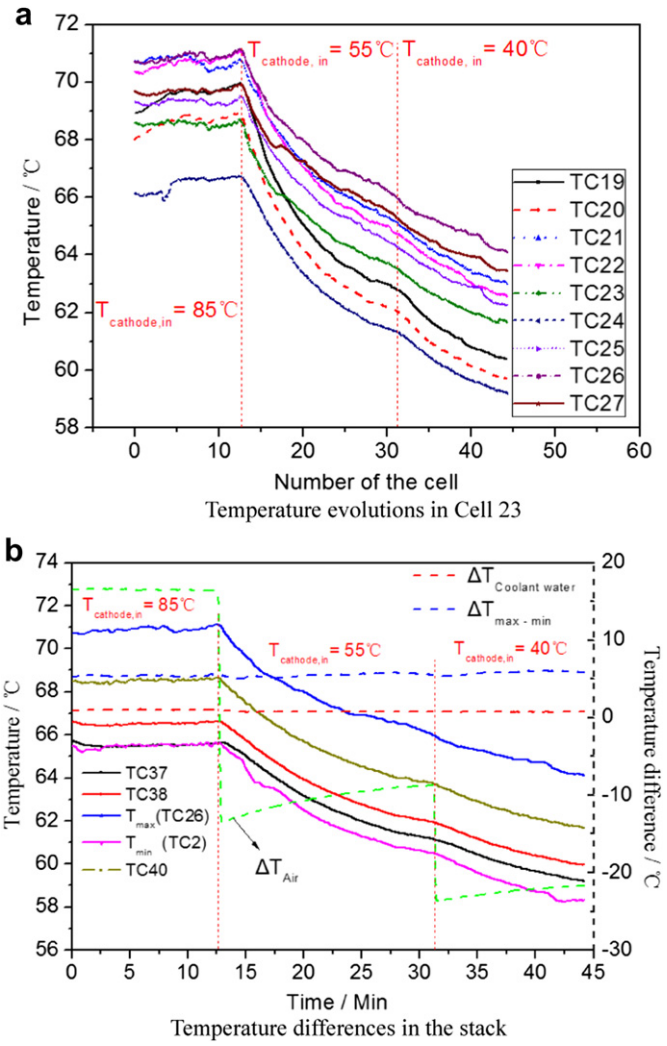

Fig. 7. Temperature distribution at different inlet air temperatures. (a) Temperature evolutions in cell 23. (b) Temperature differences in the stack.

with a value of 22 °C with respect to the inlet air temperature of 40 °C. This was attributed to the low specific heat capacity of the air which could be easily cooled or heated in the stack.

3.5. Effect of coolant water flow rate on temperature and heat distributions

Fig. 8 shows the temperature and heat distributions with different coolant water flow rates at 500 mA cm^{-2} when the hydrogen and air flow rates are 40 NLPM and 500 NLPM, respectively. At first, temperatures in the stack reached the quasi-equilibrium state. The highest temperature of TC26 maintained at 69.5 °C, and it increased with the time evolution when the coolant water flow rate varied from 30 NLPM to 15 NLPM. Meanwhile, as mentioned above, the inlet and outlet temperatures would suffer a self-regulation process during the flow rate variation, and all the monitored temperatures started to increase after 2 min when the coolant water flow rate reached a stable value of 15 NLPM. Moreover, all the temperatures still increased after the self-regulation process when the water flow rates changed from 15 NLPM to 45 NLPM since the heat exchange ability between the coolant water and the bipolar plates was enhanced at the elevated flow rate. Heat removal by the coolant water could be expressed as [32]

$$Q_c = C_{l,water}\dot{m}_{water}(T_{water,out} - T_{water,in}) \quad (1)$$

where $C_{l,water}$ was the specific heat of coolant water, $\dot{m}_{water}$ was the coolant water mass flow rate, $T_{water,in}$ and $T_{water,\ out}$ were the inlet and outlet temperatures of the coolant water. Besides, the heat generated rate in the stack by using the lower heating value could be obtained as [33,34]

$$Q = nI(1.25 - V_c) \quad (2)$$

where n was the cell number, I and V_c were the operation current and mean voltage of the stack, respectively.

Fig. 8(b) presents the heat removed amount at different coolant water flow rates. As can be seen, heat exchange between the coolant water and the bipolar plates was more sufficient at the elevated water flow rate, and more heat was removed by the coolant water with larger flow rate. However, heat removed from the stack was closely related with the stack operation performance. Relations between the mean voltage and the heat generated rate were shown in Fig. 8(c). The average voltages were 0.656 V and 0.661 V when the coolant water flow rates were 30–15 NLPM, respectively. Contrarily, it increased from 0.591 V to 0.620 V under the stable flow rate of 45 NLPM. According to Eq. (2), more generated heat should be removed from the stack. Moreover, the average heat generated in

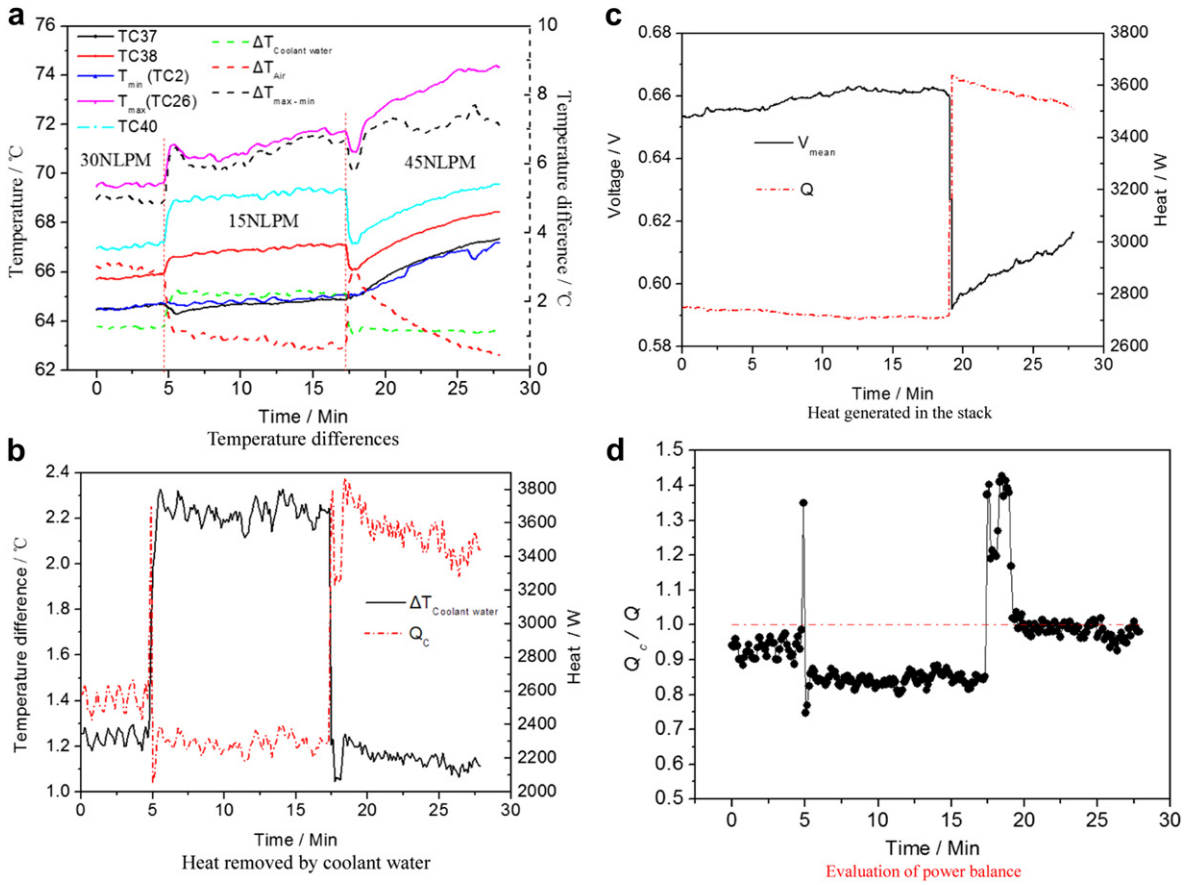

Fig. 8. Temperature and heat distributions at different coolant water flow rates. (a) Temperature differences. (b) Heat removed by coolant water. (c) Heat generated in the stack. (d) Evaluation of power balance.

the stack was 2.76 kW, 2.71 kW and 3.55 kW at the coolant water flow rates were 30 NLPM, 15 NLPM and 45 NLPM, respectively, and the heat removed by the coolant water was 2.61 kW, 2.32 kW and 3.45 kWkW. Fig. 8(d) showed the power balance of the stack at different coolant water fluxes. Heat disposal in the PEMFC was mainly determined by the coolant water and the process of water evaporation or condensation due to the exhaust streams contributed little in the heat removal [35]. At the low water flow rate of 15 NLPM, heat exchange with the bipolar plates was not so prompt that a portion of the released heat by the stack was used to help the liquid water to evaporate into water vapor. As a result, heat removal by the coolant water was about 85% in the heat generated by the stack. On the contrarily, near 97% of the released heat was removed by the coolant water due to the sufficient heat exchange between the coolant water and the bipolar plates at the elevated flow rate of 45 NLPM, and the effect of the water phase change on the heat removal could be neglected in this situation. However, evaporation and condensation processes were accompanied with absorption and release of latent heat. A comprehensive understanding of their corresponding values needed to be confirmed by more accurate real-time and in situ measurements.

4. Conclusions

Temperature distribution was investigated in a 46 fuel cells stack by embedding 36 T type thermocouples between the channel rib and the GDL surface. The conclusions can be drawn as follows,

- The highest temperature located in the bottom-middle of the single cell in the stack and the lowest temperature appeared in the top-middle. In addition, the highest temperature, lowest temperature and temperature difference at every single cell all exhibited “Parabola” distribution, and special attention should be paid in the heat exchange between the coolant water and the middle bipolar plates during the optimal design at high current densities.
- All temperatures and temperature differences at every cell increased with the increase in current density. Temperature difference decreased at a larger air flow rate and the temperature distribution was more uniform by increasing the air flow rate. However, the effect of the air inlet temperature on the temperature difference could be neglected.
- Heat generated in the stack was mainly removed by the coolant water. The heat exchange ability between the coolant water and the bipolar plates could be enhanced at the elevated coolant water flow rate, especially in the instantaneous flow concussion at the bipolar plates.

Acknowledgments

This work was supported by the National Science Foundation of China (Grant Nos. 51036003, 51106046, 50906026 and 51276071), and the Fundamental Research Funds for the Central Universities (Grant No. 2012IV084).

References

[1] Y. Yu, Z.K. Tu, Z.G. Zhan, et al., International Journal of Energy Research 36 (7) (2012) 845–855.
[2] Z.M. Wan, J.H. Wan, et al., Applied Thermal Engineering 42 (2012) 173–178.
[3] H.L. Tang, P.K. Shen, S.P. Jiang, et al., Journal of Power Sources 170 (2007) 85–92.

[4] P.Y. Yi, L.F. Peng, L.Z. Feng, et al., Journal of Power Sources 195 (2010) 7061–7066.
[5] P.Y. Yi, L.F. Peng, X.M. Lai, et al., Transactions of the ASME: Journal of the Fuel Cell Science and Technology 8 (2011) 0110111–01101110.
[6] H. Tang, S.P. Jiang, Journal of Physical Chemistry C 112 (2008) 19748–19755.
[7] W. Dai, H.J. Wang, X.Z. Yuan, et al., International Journal of Hydrogen Energy 34 (23) (2009) 9461–9478.
[8] E. Kimball, T. Whitaker, J.B. Benziger, et al., AIChE Journal 54 (2008) 1313–1332.
[9] T.S. Zhao, R. Chen, International Journal of Energy Research 35 (2011) 15–23.
[10] C.J. Bapat, S.T. Thynell, Journal of Power Sources 185 (2008) 428–432.
[11] X.G. Yang, Q. Ye, P. Cheng, International Journal of Hydrogen Energy 36 (2011) 12524–12537.
[12] J.G. Pharoah, O.S. Burheim, Journal of Power Sources 195 (2010) 5235–5245.
[13] T. Hottinen, O. Himanen, Electrochemistry Communications 9 (2007) 1047–1052.
[14] C.H. Cheng, M.H. Chang, Journal of Power Sources 139 (2005) 115–125.
[15] O.E. Herrera, D.P. Wilkinson, W. Merida, Journal of Power Sources 198 (2012) 132–142.
[16] N.A. David, P.M. Wild, J.W. Hu, et al., Journal of Power Sources 192 (2009) 376–380.
[17] S.H. He, M.M. Mench, S. Tadigadapa, Sensors and Actuators A: Physical 125 (2006) 170–177.
[18] C.Y. Lee, W.J. Hsieh, G.W. Wu, Journal of Power Sources 181 (2008) 237–243.
[19] A. Hakenjos, H. Muenter, U. Wittstadt, et al., Journal of Power Sources 131 (2004) 213–216.
[20] A. Hakenjos, C. Hebling, Journal of Power Sources 145 (2005) 307–311.
[21] R. Shimoi, M. Masuda, K. Fushinobu, et al., Journal of Energy Resources Technology 126 (2004) 258–261.
[22] M.H. Wang, H. Guo, C.F. Ma, Journal of Power Sources 157 (2006) 181–187.
[23] G. Hinds, M. Stevens, J. Wilkinson, et al., Journal of Power Sources 186 (2009) 52–57.
[24] T. Fabian, R.O. Hayre, F.B. Prinz, et al., Journal of the Electrochemical Society 154 (9) (2007) B910–B918.
[25] A.M. Abdullah, T. Okajima, A.M. Mohammad, et al., Journal of Power Sources 172 (2007) 209–214.
[26] G. Maranzana, O. Lottin, T. Colinart, et al., Journal of Power Sources 180 (2008) 748–754.
[27] C.Y. Wen, G.W. Huang, Journal of Power Sources 178 (2008) 132–140.
[28] M. Wilkinson, M. Blanco, E. Gu, et al., Electrochemical Solid-state Letters 9 (11) (2006) A507–A511.
[29] S.K. Lee, K. Ito, T. Ohshima, et al., Electrochemical Solid-state Letters 12 (9) (2009) B126–B130.
[30] P.J.S. Vie, S. Kjelstrup, Electrochimica Acta 49 (2004) 1069–1077.
[31] G.S. Zhang, L.J. Guo, L.Z. Ma, et al., Journal of Power Sources 195 (2010) 3597–3604.
[32] Y.J. Zhang, M.G. Ouyang, Q.C. Lu, et al., Applied Thermal Engineering 24 (2004) 501–513.
[33] C. Bao, M.G. Ouyanga, B.L. Yi, International Journal of Hydrogen Energy 31 (2006) 1040–1057.
[34] J. Larminie, A. Dicks, Fuel Cell Systems Explained, John Wiley & Sons Inc., New York, 2000.
[35] S.G. Kandlikar, Z. Lu, Applied Thermal Engineering 29 (2009) 1276–1280.

Nomenclature

$\Delta T_{cell\ 1}$: temperature difference in cell 1 (°C)
$\Delta T_{cell\ 11}$: temperature difference in cell 11 (°C)
$\Delta T_{cell\ 23}$: temperature difference in cell 23 (°C)
$\Delta T_{cell\ 46}$: temperature difference in cell 46 (°C)
$T_{cathode,in}$: temperature of the inlet air in the cathode (°C)
$\Delta T_{Coolant\ water}$: temperature difference between the outlet and the inlet of the coolant water (°C)
$\Delta T_{max-min}$: temperature difference between the maximal and the minimum temperature in the stack (°C)
T_{Air}: temperature difference between the inlet and the outlet temperature of the air (°C)
$\dot{m}_{water}$: mass flow rate of the coolant water (kg s^{-1})
$T_{water,in}$: inlet temperature of the coolant water (°C)
$T_{water,out}$: outlet temperature of the coolant water (°C)
$C_{l,water}$: specific heat of coolant water (J kg^{-1} $°C^{-1}$)
Q_c: heat removed by the coolant water (W)
Q: heat generated in the stack (W)
I: the operation current of the stack (A)
V_c: the mean voltage of the stack (V)